APPLIED PHYSICS LETTERS **105**, 203110 (2014)

Radioluminescence characterization of *in situ* x-ray nanodosimeters: Potential real-time monitors and modulators of external beam radiation therapy

Jeffrey S. Souris,[1,a)] Shih-Hsun Cheng,[1,3,a)] Charles Pelizzari,[2] Nai-Tzu Chen,[1,3]
Patrick La Riviere,[1] Chin-Tu Chen,[1,b)] and Leu-Wei Lo[1,3,b),c)]
[1]*Department of Radiology, The University of Chicago, Chicago, Illinois 60637, USA*
[2]*Deaprtment of Radiation and Cellular Oncology, The University of Chicago, Chicago, Illinois 60637, USA*
[3]*Institute of Biomedical Engineering and Nanomedicine, National Health Research Institutes, Zhunan, Mioli 35053, Taiwan*

(Received 9 September 2014; accepted 22 October 2014; published online 20 November 2014)

Europium-doped yttrium oxide (Y_2O_3:Eu) has garnered considerable interest recently for its use as a highly efficient, red phosphor in a variety of lighting applications that include fluorescent lamps, plasma, and field emission display panels, light emitting diodes (LEDs), and lasers. In the present work, we describe the development of Y_2O_3:Eu nanoparticles for a very different application: *in situ*, *in vivo* x-ray dosimetry. Spectroscopic analyses of these nanoparticles during x-ray irradiation reveal surprisingly bright and stable radioluminescence at near-infrared wavelengths, with markedly linear response to changes in x-ray flux and energy. Monte Carlo modeling of incident flux and broadband, wide-field imaging of mouse phantoms bearing both Y_2O_3:Eu nanoparticles and calibrated LEDs of similar spectral emission demonstrated significant transmission of radioluminescence, in agreement with spectroscopic studies; with approximately 15 visible photons being generated for every x-ray photon incident. Unlike the dosimeters currently employed in clinical practice, these nanodosimeters can sample both dose and dose rate rapidly enough as to provide real-time feedback for x-ray based external beam radiotherapy (EBRT). The technique's use of remote sensing and absence of supporting structures enable perturbation-free dosing of the targeted region and complete sampling from any direction. With the conjugation of pathology-targeting ligands onto their surfaces, these nanodosimeters offer a potential paradigm shift in the real-time monitoring and modulation of delivered dose in the EBRT of cancer *in situ*.
[http://dx.doi.org/10.1063/1.4900962]

With the recent advances in conformal proton radiotherapy (CPR) and fractionated intensity modulated radiotherapy (IMRT), there now exists the ability to target tumors and their margins with such precision as to largely spare adjacent healthy tissues from exposure.[1–6] However, even with the best treatment planning available, such target selectivity is rarely realized.[7–9] Cardiopulmonary motion, transient edema, and luminal filling and voiding of organs such as bladder and gastrointestinal (GI) tract can displace targeted pathologies, resulting in both under treatment of disease and radiation damage of normal peripheral tissues.[10–13] To compensate for such displacements, computed tomography/linear accelerator (CT/LINAC)-based image-guided radiotherapy (IGRT), on-board imaging (OBI), and cone-beam CT may be used to position the patient immediately prior to radiotherapy commencement.[13–15] But, there is still no guarantee that the targeted region will remain stationary during the entire treatment period. And, there is currently no means by which one can assess whether or not the proper dose has been delivered exactly as planned, or to what degree the delivered dose deviated from that intended. To accomplish these tasks, real-time *in vivo* dosimetry is needed.

Unfortunately, most dosimeters are not especially well suited for the real-time *in vivo* monitoring of x-ray based external beam radiotherapy (EBRT)—and none that can sample both dose and dose rate rapidly enough as to provide real-time feedback for EBRT. The most commonly used, commercially available radiation dosimeters at present are comprised of thermoluminescent detectors (TLDs), ionization chambers, silicon diodes (SiDs), metal oxide semiconductor field-effect transistor (MOSFET)-based devices, plastic scintillation detectors (PSDs), and electronic portal imaging devices (EPIDs).[16–18] None of these detectors, aside from SiDs, permits real-time measurement of dose rate. And none, aside from PSDs, are water equivalent (i.e., free of dose perturbation). TLDs and ionization chambers are not overly amenable to *in vivo* real-time monitoring, due to limitations in their size, speed, readout ease/access, and resolution.[18–20] SiDs afford real-time read-out, high sensitivity, simple instrumentation, and excellent reliability/robustness, but suffer from strong energy dependence, significant orientation sensitivity, and potential dose perturbation.[18,21–23] MOSFET-based devices exhibit excellent spatial resolution and minimal dose perturbation, but are costly, exhibit significant angular and energy dependencies, and lose sensitivity with increased absorbed dose—limiting their lifetimes to 70–200 Gy.[24–26] PSDs possess a number of favorable dosimetric characteristics that include water-equivalence, energy independence, dose linearity, quick response, and resistance

---

[a)] J. S. Souris and S. H. Cheng contributed equally to this work.
[b)] C. T. Chen and L. W. Lo contributed equally to this work.
[c)] Author to whom the correspondence should be addressed. Electronic mail: lwlo@nhri.org.tw

to radiation damage.[27,28] However, PSDs, and the plastic optical fibers through which they communicate, often generate both fluorescence and Cerenkov luminescence upon x-ray exposure, complicating dosimetric interpretation.[29,30] EPIDs, typically flat panel detectors based on amorphous silicon (a-Si) photodiode technology, also demonstrate a number of desirable dosimetric properties that include dose rate independence and approximate linearity of response with integrated dose.[18,31,32] Unfortunately, EPIDs exhibit "ghosting" (persistent signal after irradiation cessation) and are extremely sensitive to lower energy photons and thus to the non-water equivalence (attenuation) of their own construction.[32–34]

Fundamentally limiting the accuracy and utility of all the foregoing approaches is the dosimeter's lack of proximity to the target volume. In this sense, *in vivo* dosimetry is, in clinical vernacular, something of a misnomer in that one does not truly measure the deposited dose *in situ*. Indeed, the majority of *in vivo* dosimeters are placed external to the patient's body during irradiation; with the delivered dose being inferred from the incident/emergent x-ray flux so measured. In situations in which physiology does permit internal, pathology-proximal placement of the dosimeter—for example, in endoscopically or laproscopically accessible regions—significant improvements in dose accuracy can be achieved.[35–37] However, even these pathology-proximal measurements are subject to misinterpretation and error. Quite often dosimeter geometry and patient anatomy constrain measurement of delivered dose, due to the inability to completely sample—from all directions—the delivery of radiation.

To address these impediments, we have developed Y_2O_3:Eu nanoparticles that exhibit surprisingly bright, stable phosphorescence upon their x-ray irradiation—to use as *in situ* dosimeters. Spectroscopic analyses of their radioluminescent response reveals marked linearity with changes in x-ray flux and energy, making them well suited for dosimetric applications. Moreover, with the conjugation of pathology-targeting ligands onto their surfaces, these nanodosimeters offer a potential paradigm shift in the real-time monitoring of delivered dose of external beam radiation therapy—by enabling direct, non-invasive, unobstructed visualization of the dose actually delivered *to* the pathology. The technique's use of remote sensing and absence of supporting structures enable perturbation free dosing of the targeted pathology (i.e., true water-equivalence) and complete sampling from any direction. With the relatively fast excitation and short phosphorescence lifetime ($\tau = 1.07$ ms), the optical response of these *in situ*, remotely read nanodosimeters is sufficiently swift—relative to typical gantry rotation and beam translation rates of EBRT—so as to obviate afterglow concerns and permit real-time measurement of both dose rate and integrated, delivered dose and provide feedback for EBRT modulation. And our nanodosimeter's relatively narrow-band long-wavelength luminescence, centered at 610 nm, allows transport of light through tissue without being debilitated by photon absorption or scattering.

Synthesis of the Y_2O_3:Eu (2% Eu doping, by weight) nanoparticles is straightforward and accomplished via a general urea homogeneous precipitation method.[24] Typically, solutions comprised of 0.04 mol l^{-1} $Y(NO_3)_3$, 0.002 mol l^{-1} $Eu(NO_3)_3$, and 2 mol l^{-1} $(NH_2)_2CO$ were mixed together and then aged for 4 h at 85 °C, to form a light-white precipitate. The resulting precursors were then isolated by three iterations of distilled water suspension/washing, centrifugation, and supernatant extraction. Particle morphology of the so derived Y_2O_3:Eu nanoparticles was then characterized via high-resolution transmission electron microscopy (HRTEM: Hitachi H-7650), operating at an acceleration voltage of 80 kV. A typical HRTEM image of the resulting Y_2O_3:Eu nanoparticles appears in the upper-left inset of Figure 1(a); demonstrating an average particle diameter of 150 nm.

X-ray induced luminescence studies were conducted using an X-RAD 225CX Small Animal Intensity Modulated Radiation Therapy (X-RAD 225CX IMRT) System, operating at 25–225 kVp tube potential and 1–25 mA tube current, both with and without Cu (0.3 mm thick) filtering of lower energy photons. The emergent x-ray beam was collimated to a diameter of 15 mm so as to fully bathe the Y_2O_3:Eu phantom yet prevent scattering and fluorescence from neighboring support structures. For spectroscopic studies of the induced radioluminescence, 10 mg of Y_2O_3:Eu nanoparticles were placed into a 1 ml cuvette containing 250 μl distilled water that had been situated vertically, approximately 7.5 cm directly beneath the x-ray beam collimator's exit aperture, as shown in the widefield view and collimated field view (lower-left inset) of Figure 1. Emitted phosphorescence was collected by a 600 μm diameter glass bundle optical fiber positioned orthogonal to the x-ray beam and cuvette, just outside the beam path and connected to a highly compact, fluorescence spectrophotometer (USB 4000, Ocean Optics).

Monte Carlo methods, incorporating the operating parameters and physical properties of the X-RAD 225CX IMRT System, were used to estimate the x-ray photon flux impinging upon the cuvette. As shown by the phase-space plane of the collimator's exit aperture in Figure 1(b), with 140 kVp tube potential and no Cu filtration (i.e., no beam hardening), the x-ray fluence was quite uniform over the 7.5 mm × 7.5 mm central-square. Given the 1.33 magnification factor that resulted from the beam's intrinsic divergence, this region is projected onto a 1.0 cm × 1.0 cm square (cuvette cross-section) at the isocenter; with a calculated fluence of 1.179×10^{10} photons/cm^2 per mA-second. Insertion of a 0.3 mm thick slab of Cu at the collimators entrance aperture—commonly used in clinical practice to reduce x-ray dosing of superficial/intervening healthy tissues—significantly attenuated lower energy (<100 kVp) photons, as shown in Figure 1(c).

A typical radioluminescence spectra derived from this experimental configuration appears in Figure 1(d). All emission peaks that occur between 580–640 nm for Y_2O_3:Eu represent $^5D_0 \rightarrow {}^7F_J$ ($J = 0, 1, 2, 3, 4$) emission lines of Eu^{3+}, with the hypersensitive red emission $^5D_0 \rightarrow {}^7F_2$ (610 nm) transition being by far the most prominent of the group. When the Eu^{3+} ion is located at a low-symmetry site (without an inversion center), the hypersensitive $^5D_0 \rightarrow {}^7F_2$ transition is often dominant in its emission spectrum. The peaks of 587, 593, and 599 nm ($^5D_0 \rightarrow {}^7F_1$ transition) tended to coalesce into a single, broad peak centered at 590 nm, and denote principally magnetic dipole–dipole transitions that

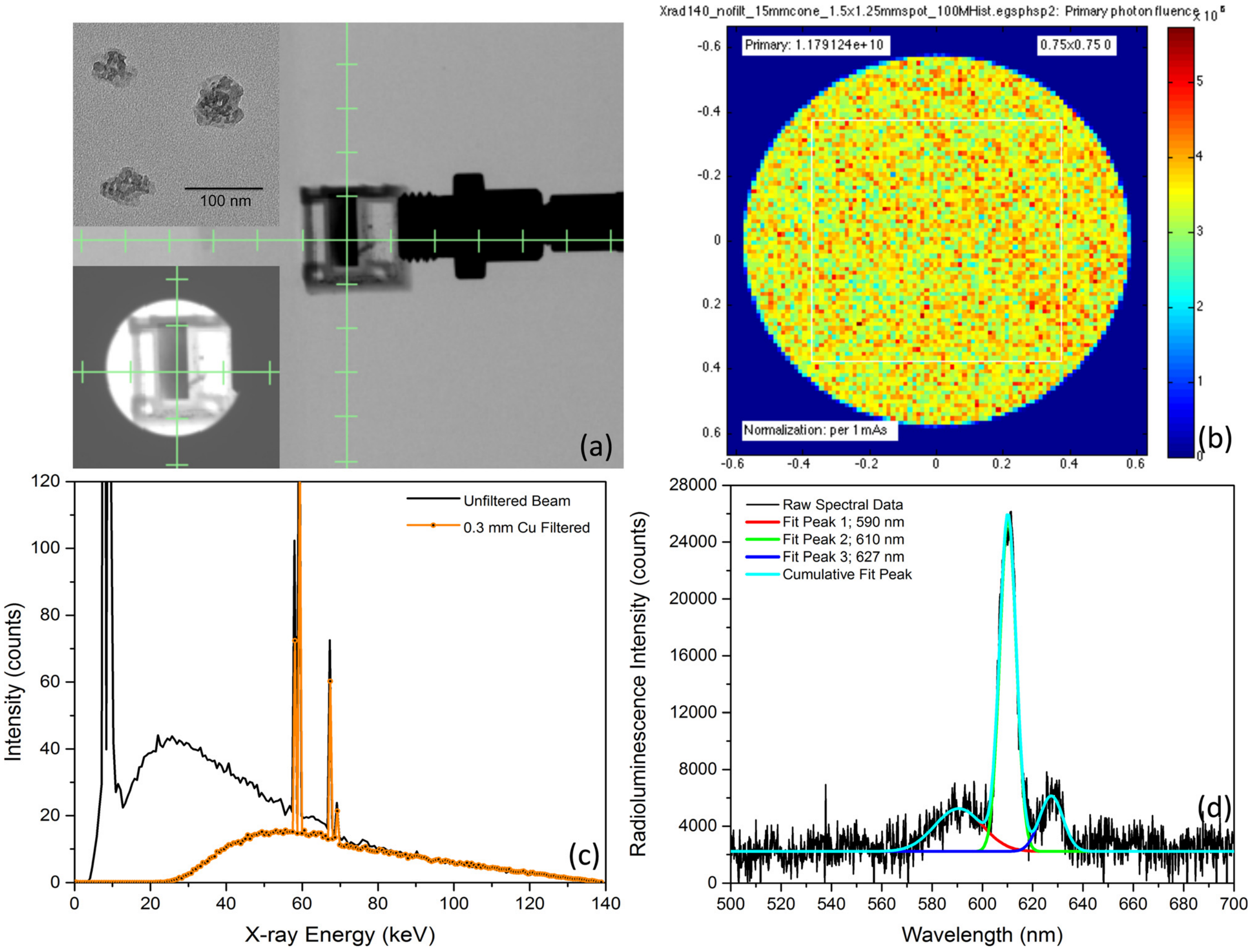

FIG. 1. (a) Uncollimated, axial projection x-ray image of Y_2O_3:Eu filled cuvette, abutted to optical bundle fiber for spectra collection during irradiation. Insets: (upper-left) HRTEM image of Y_2O_3:Eu nanoparticles with 200 nm scale bar and (lower-left) collimated view of same cuvette. (b) Monte Carlo derived phase-space plane at collimator's exit aperture, showing 1.179×10^{10} x-ray photon flux per mA-sec impinging upon isocenter for mouse phantom studies. (c) Effect upon insertion of 0.3 mm thick Cu filter upon energy spectra, clinically used to prevent patient dosing of low energy, non-therapeutic photons. (d) Typical radioluminescence spectra showing dominant emission peaks at 590 nm, 610 nm, and 627 nm, as well as their corresponding, independent Gaussian curve-fits.

are not dependent on europium ion's site symmetry. Additional spectral peaks arising from other Eu^{+3} transitions include $^5D_0 \rightarrow {}^7F_0$ (near 580 nm, convolved into the 590 nm peak) and $^5D_0 \rightarrow {}^7F_3$ (near 627 nm). Nanodosimetric consequences of the known temperature dependence of Eu^{+3} luminescence intensity, linewidth, and lifetime are minimal and static, due to the intrinsically tight thermal regulation of the *in vivo* environment and the negligible (<1 mK) temperature rise generated *in vivo* by the ionizing radiation of EBRT.[38,39]

For each tube potential selected, complete radioluminescence spectra were collected and subsequently curve-fitted (Gaussian)—to establish the peak wavelength, height, and area-under-curve (AUC) for the 590 nm, 610 nm, and 627 nm peaks, as shown in Figure 1(d). A summary plot of these various AUC integrals and their summations (ΣAUC) appears in Figure 2(a), for tube currents of 5, 10, and 20 mA. As can be seen in that figure, the integrated AUC of both the dominant 610 nm peak and the summation of the integrated AUCs of the 590 nm, 610 nm, and 627 nm peaks reveal highly linear behavior with changes in peak tube voltage (kVp) and thus, by extension, mean x-ray energy. More specifically, (a) at 20 mA tube current, $AUC_{610} = -29264.60 + 1883.06*kVp$ with $r^2 = 0.995$, while $\Sigma AUC = -49638.52 + 2895.93*kVp$ with $r^2 = 0.995$; (b) at 10 mA tube current, $AUC_{610} = -9748.04 + 1103.43*kVp$ with $r^2 = 0.997$, while $\Sigma AUC = -20136.45 + 1677.23*kVp$ with $r^2 = 0.994$; and (c) at 5 mA tube current, $AUC_{610} = 5277.91 + 473.49*kVp$ with $r^2 = 0.995$, while $\Sigma AUC = -9627.65 + 810.99*kVp$ with $r^2 = 0.990$. Although the various AUCs and, more specifically, the ΣAUC reflect what a broadband, continuously sampling photon detector senses, we were also interested in learning if just the radioluminescence's peak intensity might also serve as an accurate metric of the nanodosimeter's x-ray energy deposition and impinging flux. To this end, we graphed the 610 nm peak's radioluminescence intensity as a function of tube voltage and current, as shown in Figures 2(b) and 2(c). As can be seen in Figure 2(b), for 5, 10, and 20 mA tube currents, the dominant peak's intensity increases linearly with mean x-ray energy. More specifically, (a) at 20 mA, $I = 970.93 + 196.25*kVp$ with $r^2 = 0.998$; (b) at 10 mA, $I = -580.61 + 131.91*kVp$ with $r^2 = 0.998$; and (c) at 5 mA, $I = 714.97 + 61.77*kVp$ with $r^2 = 0.991$. Figure 2(b) also shows the intensity reduction as a function of tube voltage for the clinically relevant blockage of lower energy, non-therapeutic x-rays via the Cu filter of Figure 1(c), in which

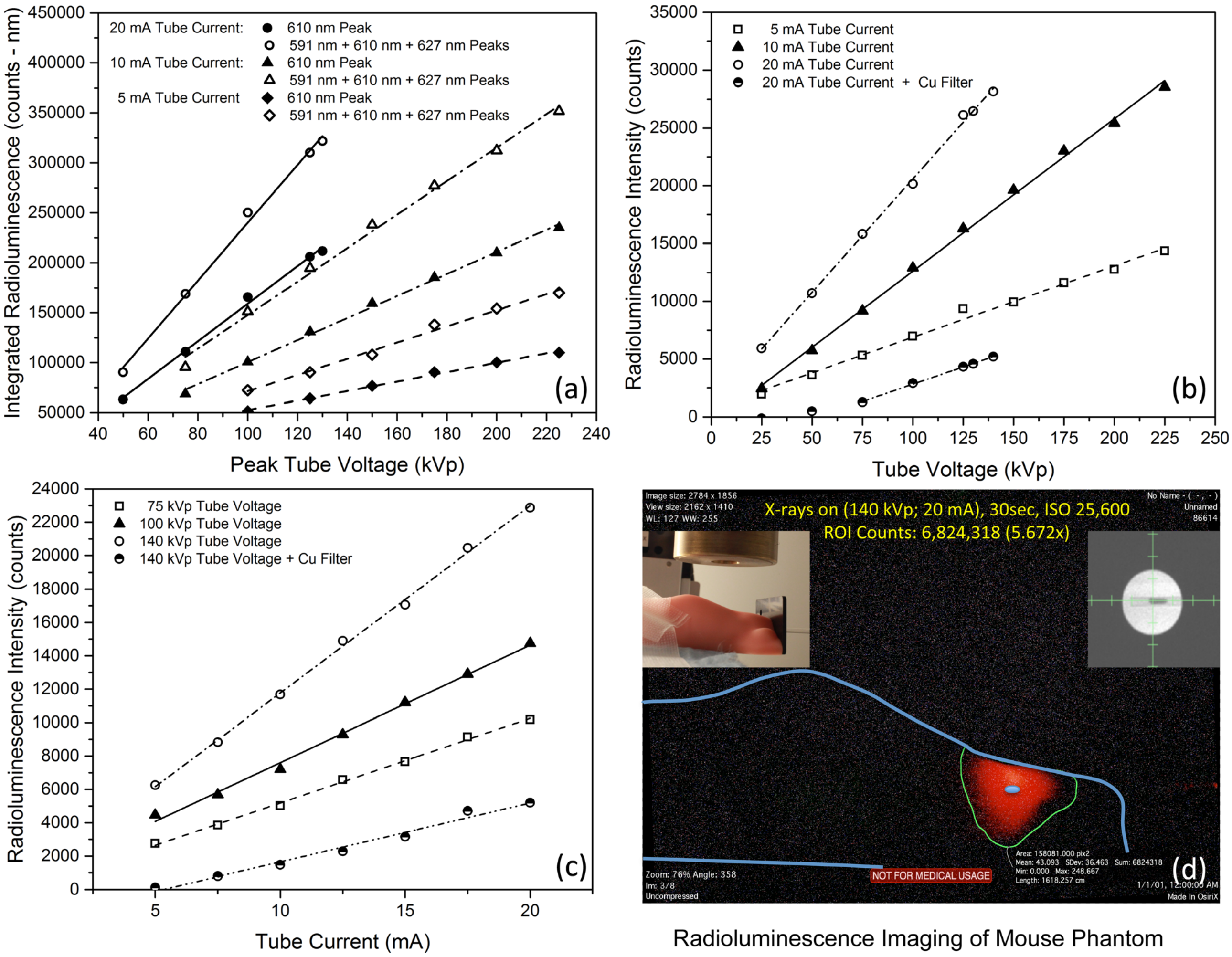

FIG. 2. (a) Area-Under-Curve of 610 nm (solid symbols) and summed (open symbols) 590 nm + 610 nm + 627 nm (open) radioluminescence spectra peaks—as a function of peak tube voltage (proportional to x-ray energy)—for various tube currents (proportional to x-ray flux), showing excellent linearity. (b) and (c) Intensity (height) of the 610 nm principal radioluminescence peak, as a function of tube voltage and current, demonstrating marked linearity for various tube currents and voltages, respectively. (d) Representative radioluminescence image of a mouse phantom (upper-left inset) into which was inserted 10 mg of Y_2O_3:Eu nanoparticles, contained within a 1.6 mm diameter borosilicate glass tube (upper-right inset).

$I = -3165.42 + 59.88*kVp$ with $r^2 = 0.999$ for $kVp > 75$, to achieve count rates of statistical significance. As can be seen in Figure 2(c), for 75, 100, and 140 kVp peak tube voltages, the 610 nm peak's radioluminescence intensity similarly increases linearly with mean x-ray photon flux. More specifically, (a) at 140 kVp, $I = 556.75 + 1121.99*kVp$ with $r^2 = 0.998$; (b) at 100 kVp, $I = 559.82 + 704.24*kVp$ with $r^2 = 0.995$; and (c) at 75 kVp, $I = 118.36 + 507.00*kVp$ with $r^2 = 0.998$. Figure 2(c) also shows the intensity reduction as a function of tube current for the clinically relevant blockage of lower energy, non-therapeutic x-rays via the Cu filter of Figure 1(c), in which $I = -1871.50 + 352.77*kVp$ with $r^2 = 0.979$. The decrease in slope of the linear fits of both radioluminescence intensity vs. tube voltage and radioluminescence intensity vs. tube current upon Cu filtration arises, we posit, from both the reduction of photon flux and the shift in the mean bremsstrahlung x-ray energy to higher energies and thus excitation of deeper Y_2O_3:Eu nanoparticles within the cuvette—whose radioluminescence (optical) signal becomes attenuated (absorbed and scattered) as it exits the sample, prior to spectroscopic detection: the inner-cell effect. Attenuation of x-ray flux alone (i.e., unchanged x-ray energy spectrum) would simply translate the Cu filtered regressions to lower intensities, resulting in the filtered and unfiltered linear fits being parallel to one another.

As an initial assessment of the feasibility of our Y_2O_3:Eu nanoparticles for *in situ* dosimetry, a 4.0 mm length of borosilicate tubing of 1.6 mm ID (2.0 mm OD) was loaded with 10 mg of Y_2O_3:Eu comprised of 1.396×10^{18} nanoparticles. The tube was then sealed and inserted 17.5 mm axially midline into a silicone mouse phantom that possessed realistic photon scattering and absorption coefficients. The cuvette was then removed from the X-RAD 225CX IMRT System and replaced with the Y_2O_3:Eu-loaded mouse phantom. A projection x-ray image was then taken to ensure placement of the Y_2O_3:Eu specimen within the collimated 15 mm diameter x-ray beam, as shown in Figure 2(d) (upper-right inset). Situated as such, the Y_2O_3:Eu specimen presented a 6.4 mm^2 cross-section (8.0 mm^3 volume) to the beam, into which 1.58×10^{10} x-ray photons/s struck (tube current = 20.89 mA, peak tube voltage = 140 kVp), based upon the Monte Carlo modeling shown in Figure 1(b). A remotely operated, 21 megapixel, Canon EOS 5D Mark II, with 35 mm F 1.4 lens (stopped down to F 8.0), was then positioned orthogonal to the x-ray beam path and mouse phantom at a distance of 15.0 cm. As can be seen from Figure 2(d), for a 30 s exposure at ISO 25 600 using this pro-consumer grade camera, significant radioluminescence signal was readily observed. To better quantify this limited view measurement, in which only 2.45% of the 4π steradian solid angle was sampled, the Y_2O_3:Eu specimen was withdrawn from the mouse phantom and replaced with a calibrated (photons/sec/cm^2/sr) light emitting diode (LED) of comparable spectral width and wavelength. Under these conditions and compensating for spectral differences in emission (but not inner-cell attenuation), comparison of the images captured of the mouse phantom bearing the calibrated LED to those of the x-ray irradiated mouse phantom bearing the Y_2O_3:Eu specimen revealed approximately 15 visible photons had been generated for every incident x-ray photon.

In summary, we have developed Y_2O_3:Eu nanoparticles that exhibit surprisingly bright, stable phosphorescence upon their x-ray irradiation; with marked linearity of response for changes in x-ray flux and energy, making them well suited for dosimetric applications. Their use of remote sensing and absence of supporting structure enables perturbation free (true water-equivalence) dosing and dose measurement of the targeted pathology during irradiation. And their relatively fast excitation and short phosphorescence lifetime are sufficiently swift so as to obviate afterglow concerns and potentially permit real-time measurement of both dose rate and delivered dose: a capability that, at present, does not exist in conventional *in vivo* dosimetry. Current efforts are focused on the *in vivo* application of these *in situ* nanodosimeters—including the conjugation of pathology-targeting ligands onto their surfaces and the use of rapid, more sensitive optical detection/imaging techniques, such as limited-view diffuse optical tomography—to improve dosimetric sensitivity and signal processing speed. As such, these nanodosimeters could offer a potential paradigm shift in the real-time monitoring and feedback modulation of delivered dose in external beam radiation therapy—enabling direct, non-invasive, unobstructed visualization of the dose actually delivered to the pathology.

Research reported in this publication was partially supported by BN-103-PP-04 and NM-103-PP-01 from the National Health Research Institutes of Taiwan; NSC102-2113-M-400-001-MY3 from the National Science Council of Taiwan; and R01CA171785, R01EB011640, P30CA14599, and S10RR026747 from the National Institutes of Health.

[1] N. C. Sheets, G. H. Goldin, A. M. Meyer, Y. Wu, Y. Chang, T. Sturmer, J. A. Holmes, B. B. Reeve, P. A. Godley, W. R. Carpenter, and R. C. Chen, JAMA, J. Am. Med. Assoc. **307**, 1611 (2012).

[2] C. M. Nutting, J. P. Morden, K. J. Harrington, T. G. Urbano, S. A. Bhide, C. Clark, E. A. Miles, A. B. Miah, K. Newbold, M. Tanay, F. Adab, S. J. Jefferies, C. Scrase, B. K. Yap, R. P. A'Hern, M. A. Sydenham, M. Emson, E. Hall, and Parsport Trial Management Group, Lancet Oncol. **12**, 127 (2011).

[3] A. Eisbruch, J. Harris, A. S. Garden, C. K. Chao, W. Straube, P. M. Harari, G. Sanguineti, C. U. Jones, W. R. Bosch, and K. K. Ang, Int. J. Radiat. Oncol., Biol., Phys. **76**, 1333 (2010).

[4] X. Zhang, Y. Li, X. Pan, L. Xiaoqiang, R. Mohan, R. Komaki, J. D. Cox, and J. Y. Chang, Int. J. Radiat. Oncol., Biol., Phys. **77**, 357 (2010).

[5] L. A. Kachnic, H. K. Tsai, J. J. Coen, L. S. Blaszkowsky, K. Hartshorn, E. L. Kwak, J. D. Willins, D. P. Ryan, and T. S. Hong, Int. J. Radiat. Oncol., Biol., Phys. **82**, 153 (2012).

[6] T. J. C Wang, N. Riaz, S. K. Cheng, J. J. Lu, and N. Y. Lee, J. Radiat. Oncol. **1**, 129 (2012).

[7] C. K. McGarry, K. T. Butterworth, C. Trainor, S. J. McMahon, J. M. O'Sullivan, K. M. Prise, and A. R. Hounsell, Phys. Med. Biol. **57**, 6635 (2012).

[8] E. Yorke, D. Gelblum, and E. Ford, AJR, Am. J. Roentgenol. **196**, 768 (2011).

[9] J. Y. Huang, D. S. Followill, X. A. Wang, and S. F. Kry, J. Appl. Clin. Med. Phys. **14**, 4139 (2013).

[10] N. H. Haripotepornkul, S. K. Nath, D. Scanderbeg, C. Saenz, and C. M. Yashar, Radiother. Oncol.: J. Eur. Soc. Ther. Radiol. Oncol. **98**, 347 (2011).

[11] A. Rimner, D. E. Spratt, M. G. Zauderer, K. E. Rosenzweig, A. J. Wu, A. Foster, E. D. Yorke, P. Adusumilli, V. W. Rusch, and L. M. Krug, Int. J. Radiat. Oncol., Biol., Phys. **90**, 394 (2014).

[12] A. Jhingran, M. Salehpour, M. Sam, L. Levy, and P. J. Eifel, Int. J. Radiat. Oncol., Biol., Phys. **82**, 256 (2012).

[13] A. S. Reese, W. Lu, and W. F. Regine, Semin. Radiat. Oncol. **24**, 132 (2014).

[14] D. A. Jaffray, in *Intraoperative Imaging and Image-Guided Therapy* (Springer, New York, 2014).

[15] D. W. Kim, S. Bae, W. K. Chung, and Y. Lee, J. Korean Phys. Soc. **64**, 1070 (2014).

[16] B. Mijnheer, S. Beddar, J. Izewska, and C. Reft, Med. Phys. **40**, 070903 (2013).

[17] K. Tanderup, S. Beddar, C. E. Andersen, G. Kertzscher, and J. E. Cygler, Med. Phys. **40**, 070902 (2013).

[18] D. A. Low, J. M. Moran, J. F. Dempsey, L. Dong, and M. Oldham, Med. Phys. **38**, 1313 (2011).

[19] B. G. Moghaddam, M. Vahabi-Moghaddam, and A. Sadremomtaz, J. Med. Phys. **38**, 44 (2013).

[20] J. F. Aguirre, R. Tailor, G. Ibbott, M. Stovall, and W. Hanson, Proceedings of the International Symposium on Standards and Codes of Practice in Medical Radiation Dosimetry (IAEA-CN-96/82 IAEA, Vienna, 2002), pp.191.

[21] A. S. Saini and T. C. Zhu, Med. Phys. **31**, 914 (2004).

[22] A. S. Saini and T. C. Zhu, Med. Phys. **34**, 1704 (2007).

[23] A. S. Saini and T. C. Zhu, Med. Phys. **29**, 622 (2002).

[24] R. Ramaseshan, K. S. Kohli, T. J. Zhang, T. Lam, B. Norlinger, A. Hallil, and M. Islam, Phys. Med. Biol. **49**, 4031 (2004).

[25] N. Jornet, P. Carrasco, D. Jurado, A. Ruiz, T. Eudaldo, and M. Ribas, Med. Phys. **31**, 2534 (2004).

[26] International Atomic Energy Agency, IAEA Human Health Report No. 8 (Vienna, Austria, 2013).

[27] L. Archambault, T. M. Briere, F. Ponisch, L. Beaulieu, D. A. Kuban, A. Lee, and S. Beddar, Int. J. Radiat. Oncol., Biol., Phys. **78**, 280 (2010).

[28] A. S. Beddar, T. R. Mackie, and F. H. Attix, Phys. Med. Biol. **37**, 1901 (1992).

[29] L. Archambault, A. S. Beddar, L. Gingras, R. Roy, and L. Beaulieu, Med. Phys. **33**, 128 (2006).

[30] M. Guillot, L. Gingras, L. Archambault, S. Beddar, and L. Beaulieu, Med. Phys. **38**, 2140 (2011).

[31] W. van Elmpt, L. McDermott, S. Nijsten, M. Wendling, P. Lambin, and B. Mijnheer, Radiother. Oncol.: J. Eur. Soc. Ther. Radiol. Oncol. **88**, 289 (2008).

[32] A. Van Esch, T. Depuydt, and D. P. Huyskens, Radiother. Oncol.: J. Eur. Soc. Ther. Radiol. Oncol. **71**, 223 (2004).

[33] S. M. Nijsten, W. J. van Elmpt, M. Jacobs, B. J. Mijnheer, A. L. Dekker, P. Lambin, and A. W. Minken, Med. Phys. **34**, 3872 (2007).

[34] K. Matsumoto, M. Okumura, Y. Asai, K. Shimomura, M. Tamura, and Y. Nishimura, Radiol. Phys. Technol. **6**, 210 (2013).

[35] T. M. Briere, M. T. Gillin, and A. S. Beddar, Med. Phys. **34**, 4585 (2007).

[36] R. D. Black, C. W. Scarantino, G. G. Mann, M. S. Anscher, R. D. Ornitz, and B. E. Nelms, Int. J. Rad. Oncol., Biol., Phys. **63**, 290 (2005).

[37] L. Wootton, R. Kudchadker, A. Lee, and S. Beddar, Phys. Med. Biol. **59**, 647 (2014).

[38] H. Peng, H. Song, B. Chen, J. Wang, S. Lu, X. Kong, and J. Zhang, J. Chem. Phys. **118**, 3277 (2003).

[39] F. H. Attix, *Introduction to Radiological Physics and Radiation Dosimetry* (Wiley-VCH Verlag GmbH & Co. KGaA, Weinheim, Ch. 1, 4 2004).